Mixed convective heat transfer of CO_2 at supercritical pressures flowing upward through a vertical helically coiled tube

Wei Zhang [a], Shuxiang Wang [b], Changda Li [a], Jinliang Xu [b,*]

[a] Beijing Key Laboratory of Multiphase Flow and Heat Transfer for Low Grade Energy Utilization, North China Electric Power University, 102206, Beijing, China
[b] School of Energy, Power and Mechanical Engineering, North China Electric Power University, 102206, Beijing, China

ABSTRACT

The mixed convective heat transfer of CO_2 at supercritical pressures inside a vertical helically coiled tube was experimentally investigated under constant heat flux conditions. Experiments were conducted at three supercritical pressures for various heat and mass fluxes. The buoyancy force was found to have two opposing effects on the heat transfer. When $Bo^* \leq 4 \times 10^{-8}$, the forced convection is dominant, and the density is only reduced at the near-wall region, which leads to flow acceleration, relaminarization of the turbulence, and deterioration of the heat transfer. When $4 \times 10^{-8} < Bo^* \leq 8 \times 10^{-7}$, as the buoyancy number increases, natural convection starts to have a positive effect on the heat transfer, and part of the heat transfer ability is recovered. When $Bo^* > 8 \times 10^{-7}$, the natural convection is fully developed, and the relaminarization of the turbulence at the near-wall region is suppressed, which enhances the heat transfer. The coupling effects of the buoyancy force, centrifugal force, and variations in the physical properties were found to determine the temperature and heat transfer coefficient distributions along the circumference edges. Based on the current experimental data, two correlations of the Nusselt number were presented.

© 2014 Elsevier Ltd. All rights reserved.

1. Introduction

Conventional chlorofluorocarbon (CFC) and hydrochlorofluorocarbon (HCFC) refrigerants are gradually being replaced by hydrofluorocarbon (HFC) refrigerants because of potential environmental concerns. HFCs have a zero ozone depletion potential (ODP) but still have a very high global warming potential (GWP). Compared to traditional CFCs, HCFCs, and HFCs, carbon dioxide (CO_2) has the advantages of zero ODP, a small GWP, non-flammability, and non-toxicity. The most remarkable feature of CO_2 is its relatively low critical temperature of 31.1 °C, which is close to and can be even lower than ambient temperatures. Conventional vapor compression systems with CO_2 operating at ambient temperature are likely to work close to and even above the critical pressure of 7.38 MPa. The thermophysical properties of CO_2 experience dramatic variations even over a small temperature interval when it crosses the pseudo-critical point, which may lead to different momentum and energy transport behaviors. This is shown in Fig. 1; for instance, the density (Fig. 1a) and dynamic viscosity (Fig. 1c) decrease sharply near the pseudo-critical temperature T_{pc}, which may change boundary layer characteristics and affect the buoyancy and flow acceleration. The specific heat capacity keeps increasing with a large slope until it reaches a peak and then decreases sharply to its normal value (Fig. 1b); this forms a large specific heat region where the heat transfer rates may be enhanced drastically. Overall, the thermal conductivity demonstrates a decreasing trend except for a local peak near the pseudo-critical temperature (Fig. 1c).

The existing experimental and theoretical correlations developed for conventional refrigerants are not suitable for CO_2; thus, the flow and heat transfer characteristics of CO_2 at supercritical pressures have gained considerable interest as a research topic. Duffy and Pioro provided a comprehensive literature review of early studies on the flow and heat transfer of CO_2 at supercritical pressures [1]. More recently, a number of experimental and numerical studies on the heat transfer to CO_2 at supercritical pressures have been conducted with horizontal tubes [2], vertical tubes [3], and mini/micro tubes or channels [4] under heating and cooling conditions. Experiments and computational fluid dynamics (CFD) modeling have been performed to examine the enhanced heat transfer to CO_2 at supercritical pressures using different technologies such as porous tubes [5] and helical wire inserts [6]. Much
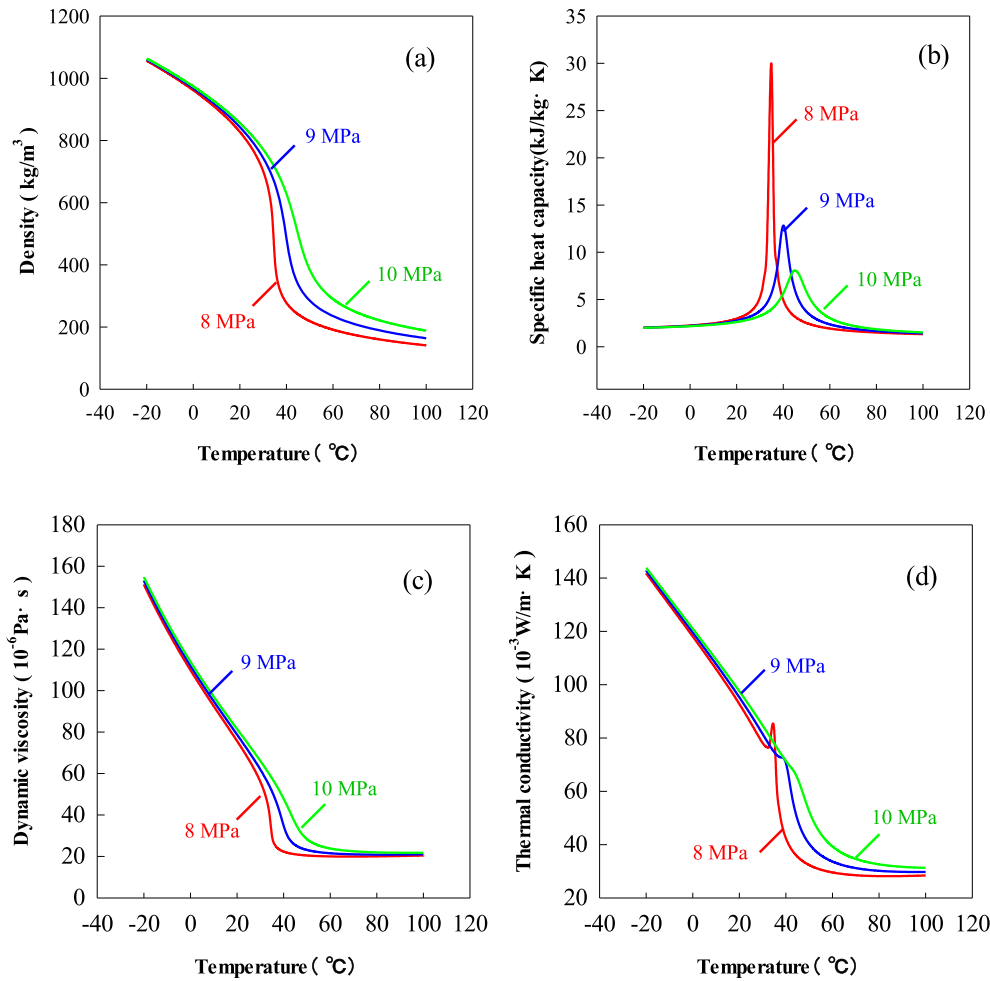
Fig. 1. Variations in physical properties of supercritical CO$_2$ near critical region: (a) density, (b) specific heat capacity, (c) dynamic viscosity, (d) thermal conductivity.

effort has gone into developing new heat transfer correlations for CO$_2$ at supercritical pressures [7].

Many of the above studies on CO$_2$ used straight tubes/channels. Little information is available on the flow and heat transfer to CO$_2$ at supercritical pressures inside helically coiled tubes. Compared to straight tubes, helically coiled tubes have higher heat and mass transfer rates because the centrifugal force caused by the curvature induces a secondary flow [8]. Numerous studies have been performed on single phase flow through a heated helically coiled tube; topics include the mixed convective effect [9] and the influence of geometric parameters [10–12]. To the authors' knowledge, very few studies have examined the flow and heat transfer behavior of CO$_2$ at supercritical pressures when it is flowing through a uniformly heated helically coiled tube. When the CO$_2$ temperature crosses the pseudo-critical point, large variations in the thermophysical properties will take place; when further coupled with the influences of geometric factors such as the curvature and torsion, this makes the heat transfer characteristics very complicated.

The objective of this study was to investigate the heat transfer characteristics of a transcritical CO$_2$ flow through a helically coiled tube under constant heat flux conditions. The effects of operating parameters including the mass flux, heat flux, and inlet pressure were considered. The coupling effects of the buoyancy force, centrifugal force, and variation of physical properties on the wall temperature and heat transfer coefficient distributions were identified and analyzed. Note that CO$_2$ has a state transition from liquid-

like to vapor-like near the pseudo-critical temperature, even though no phase change takes place [5]. The heat transfer features caused by this state transition was also analyzed. Corresponding to the fluid bulk temperatures below and above the pseudo-critical point, two new correlations of the Nusselt number were determined based on the experimental results.

2. Experiments

2.1. Experimental apparatus

Fig. 2 shows the experimental setup. The main flow loop consisted of a storage tank, plunger pump, surge tank, Coriolis mass flow meter, helically coiled tube, cooler, and back pressure valve. A bypass pipeline with a flow control valve regulated the flow rate through the helically coiled tube. Before CO$_2$ was charged, the whole flow loop was vacuumed to dissipate any non-condensable gases. A chilled water loop regulated the temperature and pressure of CO$_2$ inside the storage tank, which was maintained in a saturated state during the experiments. The plunger pump circulated CO$_2$ from the storage tank through the surge tank, Coriolis mass flow meter, helically coiled tube, cooler, back pressure valve, and finally the storage tank to complete a full cycle. The surge tank was near the outlet of the plunger pump to eliminate pressure oscillations. The cooler contained water at room temperature as the coolant to cool CO$_2$ coming from the heated test section. The back
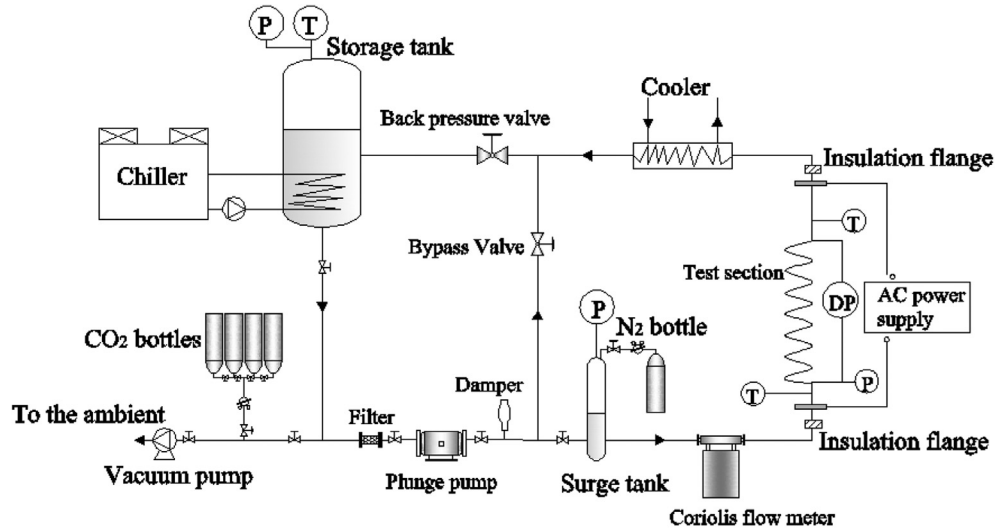
Fig. 2. Experimental setup.

pressure valve was at the outlet of the plunger pump to stabilize the outlet pressure and ensure a stable fluid flow. Two electric insulation flanges were at the two ends of the tested helically coiled tube, and two copper pads were welded between them. When an AC voltage was exerted on the two pads, the helically coiled tube was heated with a uniform heat flux.

2.2. Test section and procedures

Fig. 3a shows a schematic of the test section; Table 1 lists the geometric specifications of this section. The helically coiled tube was made of 316 stainless steel with an inner diameter of 9.05 mm, outer diameter of 12.05 mm, and length of 5500.26 mm. It
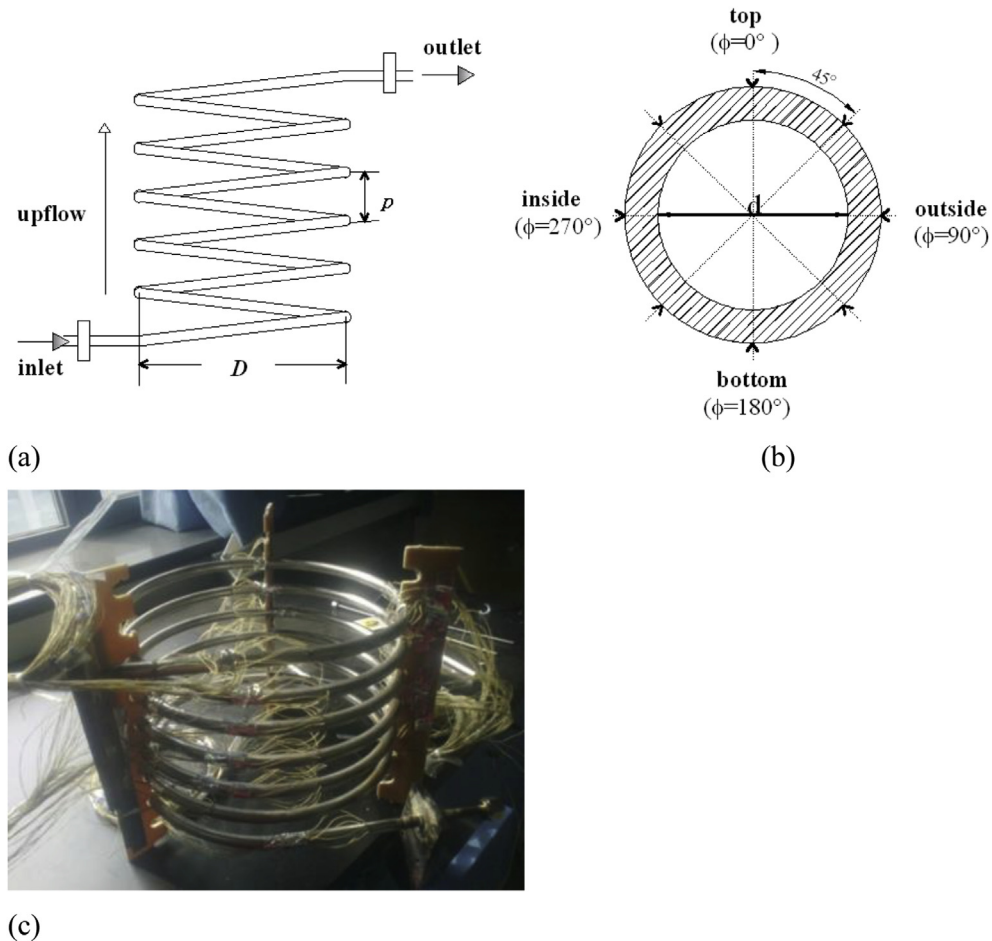

Fig. 3. Test section: (a) schematic, (b) cross-sectional thermocouple arrangement, (c) picture.

Table 1
Specifications of helically coiled tube.

Coil diameter (mm)	Inner diameter (mm)	Wall thickness (mm)	Length (mm)	Pitch (mm)	Ascending angle (°)	Number of turns
283.05	9.05	1.50	5500.26	32.05	3.2°	6

consisted of six coil turns with a coil diameter of 283.05 mm and pitch of 32.05 mm. Twenty-three cross-sections along the axial were chosen for temperature measurements. Table 2 lists the location of each cross-section, which was denoted by the relative distance from the inlet x/d; n is an integer from 1 to 23 and represents the number of the cross-section). Eight K-type thermocouples were welded at equal angle intervals of 45° along the circumference of each cross-section (Fig. 3b). Fig. 3c shows a picture of the test section. In order to reduce heat loss to the environment, a 40 mm thick glass wool insulation layer was tightly wrapped around the tested tube.

During the experiments, the helically coiled tube was placed vertically, and CO_2 flowed upward inside. The tests were conducted while varying the mass and heat fluxes at given pressures. The outlet temperature of the test section was restricted to below 120 °C to prevent thermal aging of the Teflon insulator between the flanges. During the tests, the inlet temperature was fixed at 15 °C to maintain a subcooled fluid flow at the inlet. The heat fluxes were gradually increased at the given mass flux until the temperature at the outlet exceeded the pseudo-critical point, which ensured the occurrence of transcritical flow inside the test section. All of the measured temperatures were recorded with ADAM-4118 modules. The inlet pressure and pressure drop across the test section were recorded with an Agilent HP34970A data logger system.

2.3. Data reduction

The heat flux applied to the test section was calculated by

$$q = \frac{\eta UI}{\pi dL} \tag{1}$$

where U and I are the applied voltage and current, respectively, and η is the thermal efficiency of the heating unit (determined as 0.90 from a series of thermal balance experiments with single-phase water flow). Since the heat flux was uniform, the local enthalpy increased linearly along the flow direction and was calculated by

$$H_b(n) = H_{in} + \frac{\eta UI}{L}x(n) \tag{2}$$

where H_{in} is the inlet enthalpy; n is the number of the cross-section, as listed in Table 2; and $x(n)$ is the distance from the inlet to cross-section n. The local average bulk temperature $T_b(n)$ at the given enthalpy $H_b(n)$ and operating pressure $P(n)$ was calculated by

Table 2
Locations of the cross-section for temperature measurement.

n	x/d	n	x/d	n	x/d
1	4.6	9	160.5	17	354.2
2	17.3	10	185.0	18	380.1
3	30.0	11	211.0	19	404.7
4	40.9	12	232.7	20	426.6
5	64.6	13	257.2	21	497.0
6	89.4	14	281.7	22	554.6
7	114.7	15	308.1	23	604.2
8	136.4	16	328.1		

using the NIST package [13]. The inner wall temperature was derived from the directly measured outer wall temperature by using the space-marching method for inverse heat conduction problems [14]. The local average inner wall temperature at cross-section n was calculated by

$$T_{w,inn}(n) = \frac{\sum\limits_{i=1}^{8} T_{w,inn}(n,i)}{8} \tag{3}$$

The local heat transfer coefficient was calculated by

$$h(n,i) = \frac{q}{T_{w,inn}(n,i) - T_b(n)} \tag{4}$$

The average heat transfer coefficient at cross-section n was computed by

$$h(n) = \frac{\sum\limits_{i=1}^{8} h(n,i)}{8} \tag{5}$$

2.4. Measurements and uncertainties

The outer wall temperatures were measured with 0.2 mm diameter K-type thermocouples having an uncertainty of 0.2 °C. At the inlet and outlet of the test section, two armored T-type thermocouples were inserted into the center of the bulk fluid for temperature measurement; the uncertainty was 0.2 °C. The inlet pressure and pressure drop across the test section were measured with a Rosemount 3051 pressure transmitter and pressure drop transducers having uncertainties of 0.1% and 0.05%, respectively. The mass flow rate was measured with a Coriolis mass flow meter having an uncertainty of 0.2%. The voltage and current applied to the tested tube were measured with two transformers each having an uncertainty of 0.2%. The heat transfer coefficients are indirectly measured parameters, and their uncertainty was estimated by the error propagation method [15]. The maximum uncertainties of the heat transfer coefficients and Nusselt numbers for the present experiment were calculated to be 9.7% and 9.75%, respectively.

2.5. Experimental setup validation

In order to validate the experimental setup, a series of tests was conducted with single-phase water flowing through the uniformly heated tested tube. The tests covered both laminar and turbulent flow regions. In the laminar flow region, the two correlations of the Nusselt number proposed by Dravid et al. [16] and Xin and Ebadian [17] were compared with the measured values. In the turbulent flow region, the correlations presented by Merkel [18] and Rogers and Mayhew [19] were selected for the comparison. As shown in Fig. 4, 90% of the experimental values fell within ±20% of the predicted values, which indicates that the results obtained with this experimental setup were reasonably accurate.

3. Results and discussions

The experiments were conducted at three inlet pressures of 8.02, 9.03, and 10.05 MPa under uniform heat flux conditions. The mass flow rate was 0–650 kg/m² s, and the heat flux was 0.4–50 kW/m². The inner wall temperature distributions and general heat transfer characteristics were examined. Particular focus was given to the coupling effects of the buoyancy force, centrifugal force, and variation in the thermophysical properties on the mixed convective heat transfer behavior.
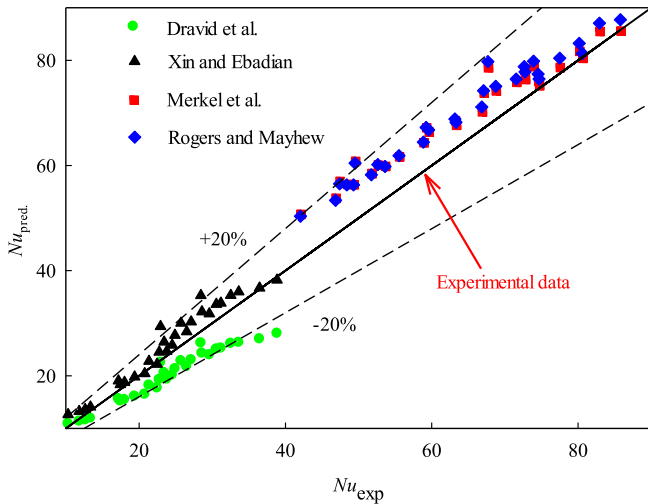
Fig. 4. Experimental apparatus validation with deionized water as working fluid. The bold solid line represents the experimental data.

3.1. Wall temperature distributions

Fig. 5 shows the inner wall temperature distributions at P_{in} = 8.02 MPa, G = 97.8 kg/m^2 s, and q = 9.03 kW/m^2. Three cross-sections along the flow direction were chosen for the analysis at x/d = 64.6, 160.5, and 354.2. The inner wall temperature along the generatrix (corresponding to a certain angle in Fig. 5) kept increasing. The inner wall temperature distribution along the circumference of each cross-section displayed an inverted parabolic shape; the lowest temperature occurred at ϕ = 135°. This temperature distribution was attributed to the coupling effects of the buoyancy and centrifugal forces. When CO_2 was heated inside the tube, the density difference at the cross-section kept increasing until it reached its peak near the critical region. The density difference led to the buoyancy effect, for which the intensity was determined by the temperature difference at the cross-section. The secondary flow structures caused by the centrifugal effect and the buoyancy effect were illustrated in Fig. 6. Fig. 6a shows the secondary flow structures induced by the individual effect of the centrifugal force, which tended to make the outside of the heated tube (Fig. 3b, ϕ = 90°) have the lowest temperature [20]. For the indivi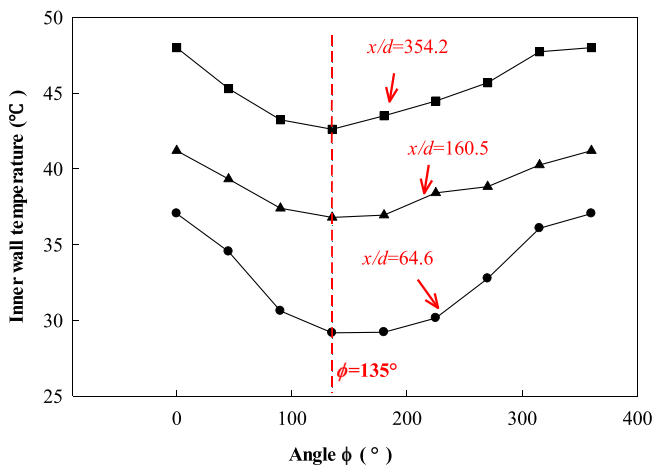dual effect of buoyancy effect inside a curved tube, natural convection was the dominant heat transfer mode and the induced secondary flow (Fig. 6b) caused the lowest temperature to occur at the bottom (Fig. 3b, ϕ = 180°) of the heated tube [21]. Fig. 6c presents a schematic of the flow structures at the cross-section of a heated helically coiled tube, where the combined effects of the buoyancy and centrifugal forces caused the lowest temperature to occur between the bottom and outside (Fig. 5; ϕ = 135°).

3.2. General heat transfer characteristics

The bulk enthalpy linearly increased along the flow direction under constant heat flux conditions. In order to determine the heat transfer mechanisms near the pseudo-critical point, the bulk enthalpy (H_b) was adopted as the x-coordinate instead of the distance from the inlet (x or x/L). Fig. 7 shows the general characteristics of the average heat transfer coefficient versus the bulk enthalpy. The heat transfer coefficient experienced a slight decrease near the inlet and then kept increasing until it peaked at 1920.38 W/m^2 K. After the peak, the heat transfer coefficient decreased with further increasing bulk enthalpy. The decrease in the heat transfer coefficient at the inlet was caused by the development of a thermal boundary layer when the subcooled CO_2 entered the heated tube. The consequent enhancement of the heat transfer with the increased bulk enthalpy can be explained by three mechanisms. At a relatively low bulk enthalpy, the physical properties do not change drastically, and the centrifugal force induces a secondary flow that dominates the heat transfer enhancement. When the bulk enthalpy increases, the inner wall temperature exceeds the pseudo-critical point, and CO_2 at the near-wall regime enters the large heat capacity region (liquid-like state), where the increase in the heat capacity of CO_2 is the main factor that enhances the heat transfer. The fluid temperature at the cross-section is non-uniform and spans the pseudo-critical point, which results in very large variations in the physical properties. The buoyancy effect induced by the large density differences at the cross-section causes a secondary flow, which strengthens the heat transfer. Thus, the three mechanisms for heat transfer are (1) a secondary flow induced by the centrifugal force, (2) a secondary flow induced by the buoyancy force, and (3) the increase in the specific heat capacity as the CO_2 approaches the pseudo-critical temperature.

The maximum heat transfer coefficient of 1920.38 W/m^2 K occurred at the bulk enthalpy of 275.76 kJ/kg; this corresponded to the state where the inner wall temperature was higher than the pseudo-critical point and the bulk temperature was approaching but still less than the pseudo-critical point. A further increase in the bulk enthalpy caused more of the fluid to enter the supercritical state and decreased the density differences at the cross-section, which weakened the secondary flow induced by the buoyancy force. On the other hand, the continuous decrease in the density accelerated the flow, which led to flow relaminarization of the turbulence and decreased the heat transfer. With continuous heat input and the corresponding bulk enthalpy increase, the state transition of CO_2 at supercritical pressures from liquid-like to vapor-like first occurred at the near-wall region, where a fluid layer with low thermal conductivity and heat capacity formed. This vapor-like fluid layer weakened the heat transfer from the inner wall to the liquid-like central liquid. When both the inner wall temperature and bulk temperature of CO_2 surpassed the pseudo-critical point, all of the fluid inside the tube turned into the vapor-like supercritical state, and the decreases in the heat conductivity and heat capacity caused the deterioration in the heat transfer.

Fig. 8 shows the state transition for transcritical CO_2 flowing through a uniform heated tube. The subcooled CO_2 flowed into the tested tube (Fig. 8a) and was heated up until the fluid near the inner

Fig. 5. Inner wall temperature distributions (P_{in} = 8.02 MPa, G = 97.8 kg/m^2 s, q = 9.03 kW/m^2).
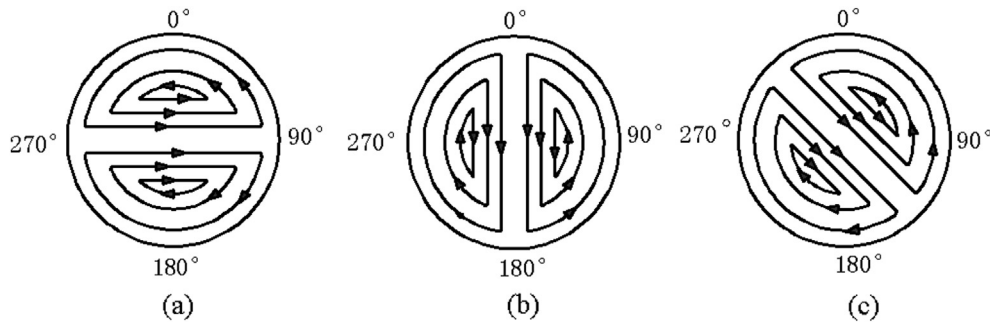
Fig. 6. Schematic of secondary flow structures caused by (a) centrifugal force, (b) buoyancy force, and (c) combination of centrifugal and buoyancy forces.

wall approached the pseudo-critical point; the liquid near the wall first turned into a liquid-like state, but the liquid inside was still subcooled (Fig. 8b). Because of the large heat capacity of the liquid-like CO_2, the heat transfer coefficient increased. Fig. 8c illustrates the state where the fluid near the wall turned from the liquid-like state to the vapor-like state with a further increase in the bulk enthalpy to form a fluid layer with a low heat capacity. The liquid-like fluid stayed adjacent to the vapor-like fluid layer, which could contain subcooled CO_2. The heat transfer was weakened by the presence of the vapor-like fluid layer at the near-wall region. Fig. 8d shows a state where the vapor-like region near the wall increased in size, and the subcooled fluid in the center disappeared. The increase in size of the vapor-like fluid region further reduced the heat transfer. As shown in Fig. 8e, the fluid inside the tube completely turned into the vapor-like state with continuous heat input and increasing bulk temperature.

3.3. Nusselt number for transcritical flow and heat transfer

The Nusselt number, which is defined as the ratio of convective heat transfer to conductive heat transfer, is usually used as an indicator of heat transfer performance. However, this was not found to be true for the convective heat transfer of transcritical CO_2. Fig. 9 shows the variation in the Nusselt number with increasing bulk temperature. Compared to Fig. 7, the Nusselt number experienced a similar process as the heat transfer coefficient for the bulk temperature below the pseudo-critical point. However, it increased sharply after the bulk temperature passed the pseudo-critical point. This phenomenon was opposite to the heat transfer variation

shown in Fig. 7, where the heat transfer coefficient decreased after the pseudo-critical temperature. The increase in the Nusselt number after the pseudo-critical temperature was induced by the decrease in the heat conductivity of CO_2; it does not reflect the real heat transfer performance but only the relative importance of convective heat transfer to conductive heat transfer.

3.4. Effect of operating parameters

The effect of the mass flux on the inner wall temperature, bulk temperature of CO_2, and heat transfer coefficient was investigated at $P_{in} = 8.02$ MPa and $q = 20.5$ kW/m². Increasing the mass flux clearly decreased the inner wall temperature and bulk temperature (Fig. 10a). When the mass flux was increased from 206 kg/m² s to 262 kg/m² s, the inner wall temperature at the outlet decreased from 78 °C to 56 °C, and the bulk temperature at the outlet decreased from 55 °C to 41 °C. The heat transfer coefficient increased with the mass flux. When the mass flux was increased from 206 kg/m² s to 262 kg/m² s, the peak of the heat transfer coefficient increased from 1690 W/m² K to 1980 W/m² K (Fig. 10b).

Fig. 11 displays the effect of the heat flux on the inner wall temperature, bulk temperature of CO_2, and heat transfer coefficient at $P_{in} = 8.02$ MPa and $G = 97.92$ kg/m² s. The inner wall temperature and bulk temperature clearly increased with the heat flux (Fig. 11a). At a relatively low heat flux of 1.65 kW/m², both the bulk temperature and inner wall temperature increased linearly along the tested tube. Because the outlet temperature was still below the pseudo-critical point, the single-phase convective heat transfer was dominant. The increase of the heat transfer coefficient was caused by the enhanced turbulence due to the reduction in viscosity and the secondary flow induced by the centrifugal effect. When the heat flux was increased until the outlet temperature exceeded the pseudo-critical temperature, the peak of the heat transfer coefficient occurred when the inner wall temperature was higher but the bulk temperature was still lower than the pseudo-critical temperature. As shown in Fig. 11b, the peak value of the heat transfer coefficient increased from 1128 W/m² K to 1310 W/m² K when the heat flux was increased from 9.03 kW/m² to 12.13 kW/m². Furthermore, increasing the heat flux produced different heat transfer characteristics for the bulk temperature below and above the pseudo-critical point. When the bulk temperature was lower than the pseudo-critical temperature, the heat transfer coefficient increased with the heat flux. However, when the bulk temperature was higher than the pseudo-critical temperature, increasing the heat flux reduced the heat transfer. This was attributed to the lower heat conductivity of supercritical CO_2 at a higher bulk temperature.

Fig. 12 shows the effect of the operating pressure on the inner wall temperature, bulk temperature, and heat transfer coefficient. When the operating pressure was increased from 8.02 MPa to 9.03 MPa, the wall temperature and bulk temperature increased
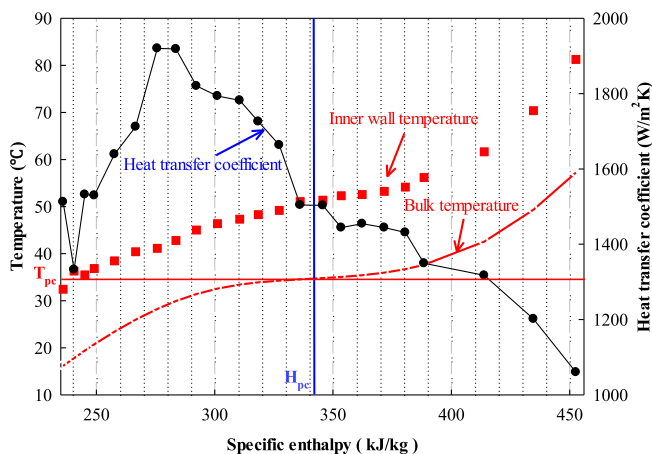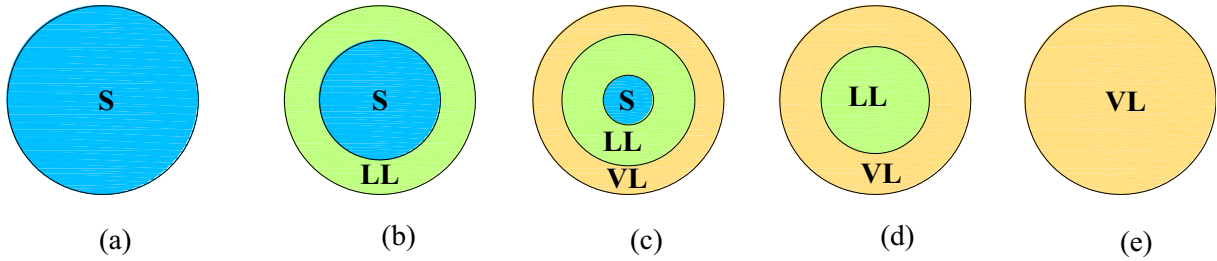

Fig. 7. General heat transfer characteristics ($P_{in} = 8.02$ MPa, $q = 25.32$ kW/m², $G = 261.6$ kg/m² s).

Fig. 8. Schematic of fluid state transition at the tube cross-section: (a) subcooled (S) CO_2 fills the whole cross-section; (b) subcooled CO_2 in the center surrounded by liquid-like (LL) CO_2 near the inner wall; (c) the most outside is vapor-like (VL) CO_2, the medium is liquid-like CO_2 and the subcooled CO_2 might exist in the center; (d) liquid-like CO_2 surrounded by vapor-like CO_2 and (e) vapor-like CO_2 occupies the full cross-section.

(Fig. 12a), but the peak value of the heat transfer coefficient decreased from 1410 W/m^2 K to 915 W/m^2 K (Fig. 12b). This was because the influence of the large heat capacity on the heat transfer weakened when the operating pressure moved away from the critical pressure (Fig. 1b).

3.5. Effect of buoyancy on heat transfer

In order to identify the effect of the buoyancy force on the heat transfer, the dimensionless buoyancy number Bo^* proposed by Jackson et al. [22] was adopted, which is defined as

$$Bo^* = \frac{Gr^*}{Re^{3.425}Pr^{0.8}} \qquad (6)$$

The buoyancy number represents the ratio of the buoyancy force to the inertial force. McEligot and Jackson [23] believed that the buoyancy effect is strong enough to result in mixed convection when the buoyancy number $Bo^* > 6 \times 10^{-7}$. In a recent paper by Jackson and his colleagues [24], they also pointed that the onset and magnitude of the maximum buoyancy effect differ between circular tubes, annuli and rectangular ducts. To determine the influence of the buoyancy effect on the heat transfer performance in the current experiments, the ratio of the heat transfer coefficients h_{exp}/h_{fc} versus $\log_{10}(Bo^*)$ was used as the coordinates for further analysis, where h_{exp} is the experimentally obtained heat transfer coefficient and h_{fc} is the heat transfer coefficient of forced convection without the buoyancy effect. The latter can be calculated by

$$h_{fc} = \frac{Nu_{fc}\lambda}{d} \qquad (7)$$
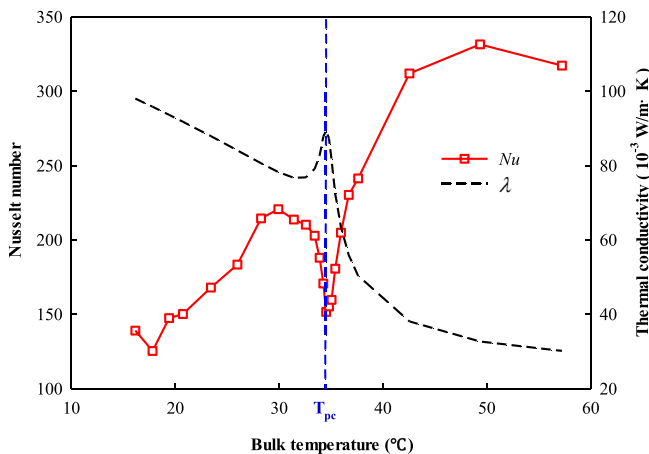
Fig. 9. Variations in Nusselt number versus bulk temperature (same case as in Fig. 7).
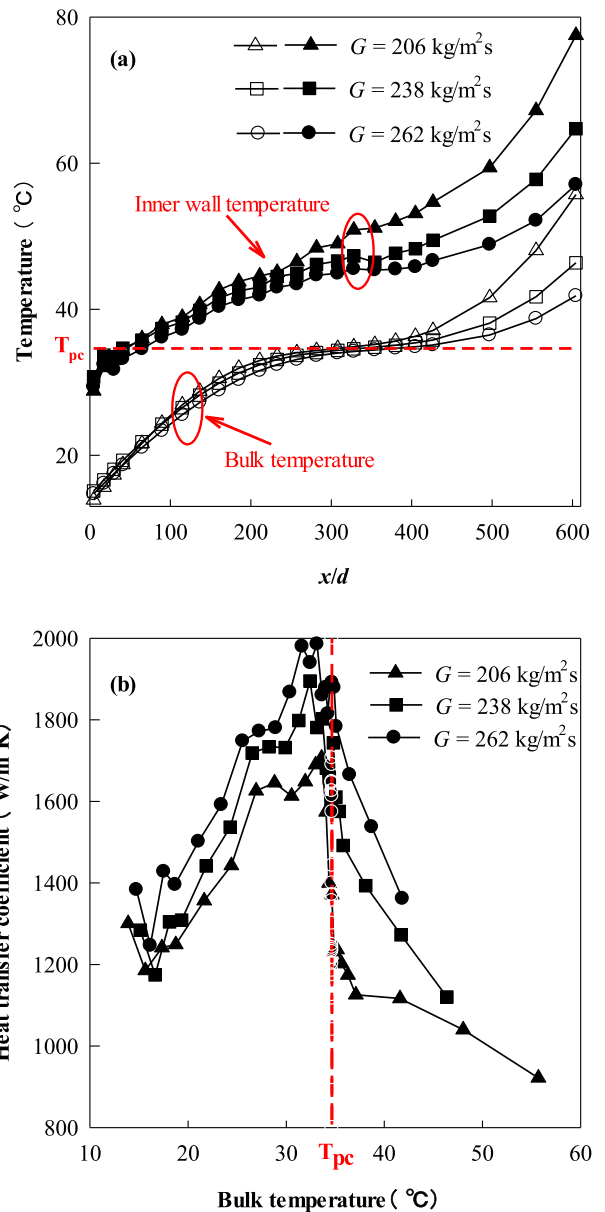
Fig. 10. Effect of mass flux on temperature and heat transfer coefficient for P_{in} = 8.02 MPa and q = 20.5 kW/m^2: (a) temperature along flow direction; (b) heat transfer coefficient versus bulk temperature.
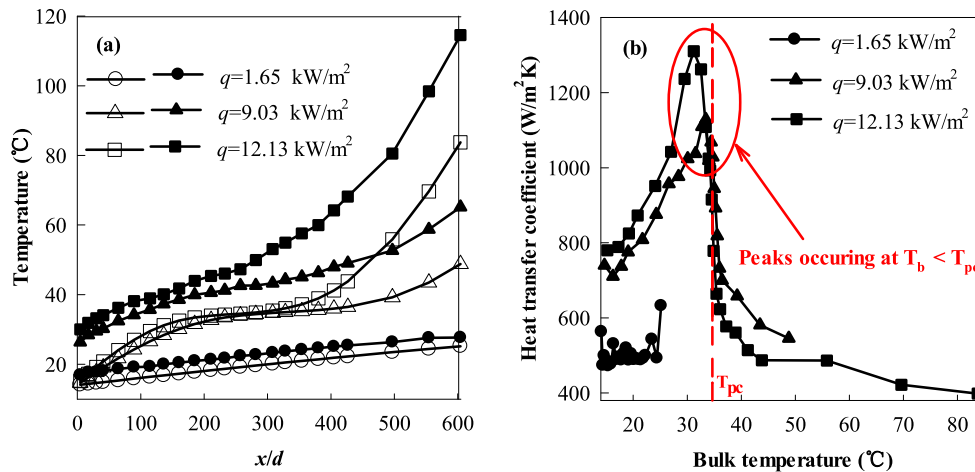
Fig. 11. Effect of heat flux on temperature and heat transfer coefficient for P_{in} = 8.02 MPa and G = 97.92 kg/m²s: (a) temperature along flow direction (the solid marks stand for the inner wall temperatures and the hollow marks stand for the bulk temperatures); (b) heat transfer coefficient versus bulk temperature.
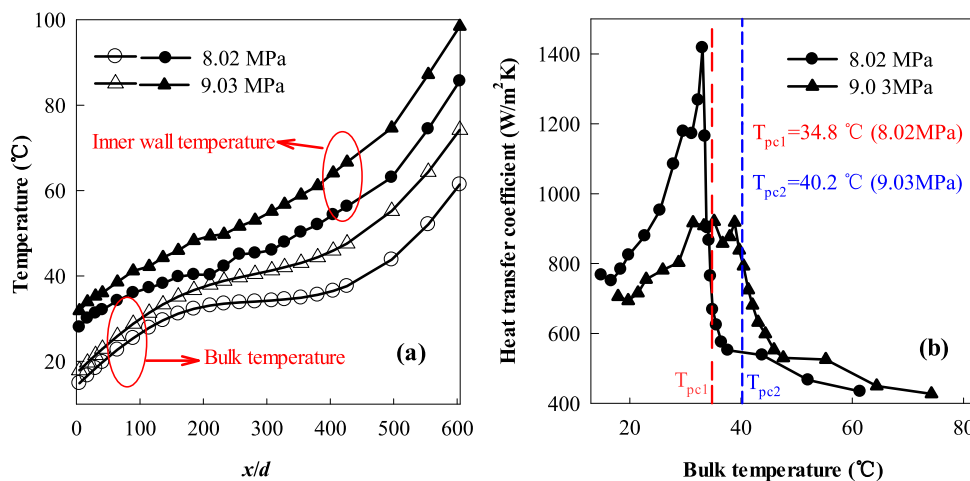

Fig. 12. Effect of operating pressure (G = 97.92 kg/m²s, q = 10.4 kW/m²).

where the Nusselt number of forced convection Nu_{fc} is calculated by Ref. [18]

$$Nu_{fc} = 0.023Re^{0.8}Pr^{0.4}(1 + 3.54\, d/D) \qquad (8)$$

Fig. 13 shows that the ratio of the heat transfer coefficients continuously decreased with increasing buoyancy number when $Bo^* \leq 4 \times 10^{-8}$. A further increase in the buoyancy number led to heat transfer recovery. When $Bo^* > 8 \times 10^{-7}$, the buoyancy effect enhanced heat transfer.

The buoyancy effect on the heat transfer can be explained by two mechanisms that lead to opposite effects. When $Bo^* \leq 4 \times 10^{-8}$, the buoyancy effect is small, and the natural convection is not strong enough to influence heat transfer. Thus, the forced convective heat transfer is dominant inside the tested tube. In this case, the density reduction due to heating only takes place near the inner wall, which lead to thermal flow acceleration and the relaminarization of turbulence at the near-wall region, weakening the heat transfer. With an increased buoyancy number, the buoyancy force strengthens, and the natural convection starts to have a positive effect on the heat transfer. At a moderate buoyancy number of $4 \times 10^{-8} < Bo^* \leq 8 \times 10^{-7}$, the heat transfer capability recovered by the natural convection is still weak and cannot fully offset the heat transfer deterioration due to the relaminarization of

turbulence. When $Bo^* > 8 \times 10^{-7}$, the natural convection is fully developed, and the relaminarization of turbulence at the near-wall region is suppressed; thus, the heat transfer is drastically enhanced.
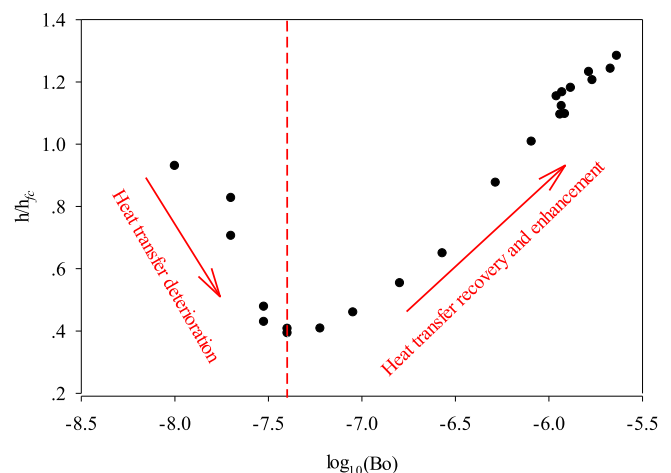

Fig. 13. Effect of buoyancy force on heat transfer characteristics.

3.6. Correlations of Nusselt number

The thermophysical properties of CO_2 near the pseudo-critical temperature experience dramatic changes, which further induce sharp variations in heat transfer characteristics. In order to capture the features of such sharp variations, more thermocouples have to be arranged at the near pseudo-critical region. However, it is very difficult to prejudge where the near pseudo-critical region locates along the axial direction. This is because the location of the near pseudo-critical region varies with the input heating power. With increasing heating power, the near pseudo-critical region will move toward the upstream of the helically tube. The thermocouples have usually been distributed with equal space along the axial direction, and they may fail to capture enough data at the near pseudo-critical region. Considering that most data obtained are corresponding to the temperatures above or below the pseudo-critical point, it is good to separate the region above and below the pseudo-critical temperature for the new correlation development. Because the variation in thermophysical properties of CO_2 is great, the terms of specific heat and density ratios are introduced into the new proposed correlations of the Nusselt number [25].

For the low enthalpy region below the pseudo-critical temperature,

$$Nu = 0.32\, Re_b^{0.55}\, Pr_b^{0.35} \left(\frac{\rho_w}{\rho_b}\right)^{0.11} \left(\frac{\overline{c_p}}{c_{\mathrm{pb}}}\right)^{0.37}, \; T_b < T_{\mathrm{pc}} \tag{9a}$$

For the high enthalpy region below the pseudo-critical temperature,

$$Nu = 0.034\, Re_b^{0.77} Pr_b^{0.57} \left(\frac{\rho_w}{\rho_b}\right)^{0.40} \left(\frac{\overline{c_p}}{c_{\mathrm{pb}}}\right)^{0.84}, T_b > T_{\mathrm{pc}} \tag{9b}$$

where the subscripts b and w represent the physical properties corresponding to the bulk temperature and inner wall temperature, respectively, and $\overline{c}_p$ is the average heat capacity that is computed by $(H_w - H_b/T_w - T_b)$.

Fig. 14 shows the uncertainties of the Nu correlations based on the current experiments. Of the experimental data, 92% fell within 20% of the values predicted by Eq. (9a) for the low enthalpy region and 93% fell within 15% of the values predicted by Eq. (9b) for the high enthalpy region. Eqs. (9a) and (9b) were developed based on experimental data using P_{in} of 8.02–10.05 MPa, G of 0–650 kg/m² s, and q of 0.4–50 kW/m². More experimental and theoretical studies are needed over a wide data range and using different geometric structures in order to develop correlations for general use.

4. Conclusions

The mixed convective heat transfer of CO_2 at supercritical pressures inside a vertical helically coiled tube was experimentally investigated under constant heat flux conditions. Experimental tests were conducted at three supercritical pressures of 8.02, 9.03, and 10.05 MPa. The heat flux was 0.4–50.0 kW/m², and the mass flux was 0–650.0 kg/m² s. The following conclusions were drawn:

1) The lowest wall temperature along the tube circumference was between the bottom and outside; this was caused by the combined effects of the buoyancy and centrifugal forces.
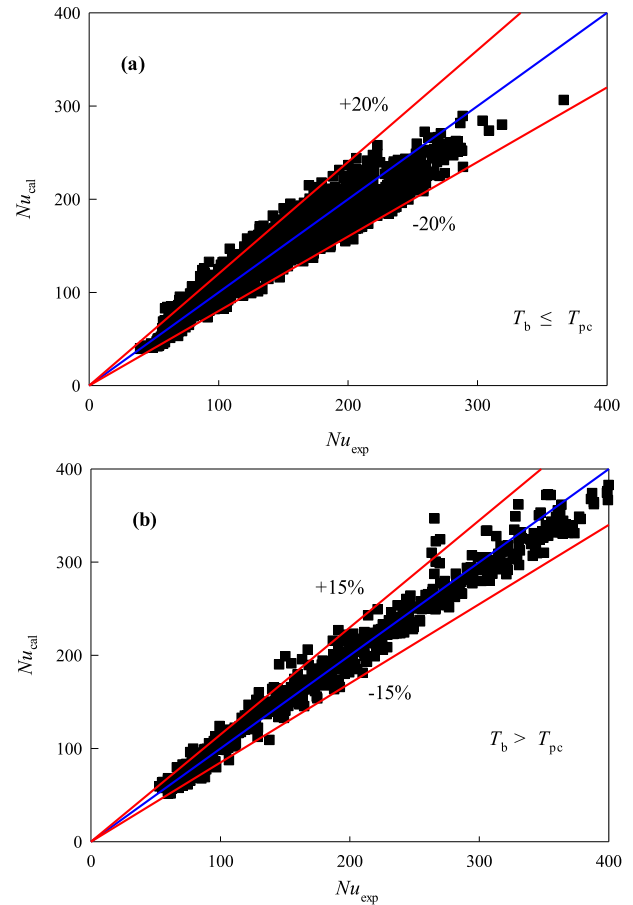2) Three mechanisms for heat transfer enhancement and two mechanisms for heat transfer deterioration were identified

Fig. 14. Comparison between predicted and experimental values of Nu when (a) $T_b \leq T_{\mathrm{pc}}$ and (b) $T_b > T_{\mathrm{pc}}$.

when the bulk enthalpy was increased from the subcooled state to the supercritical state. The heat transfer enhancement mechanisms include (a) a secondary flow induced by the centrifugal force during forced convection, (b) a secondary flow resulting from the buoyancy force during mixed convection, (c) and the large heat capacity near the pseudo-critical temperature. The mechanisms for heat transfer deterioration include (a) weakening of the secondary flow induced by the buoyancy force because of the decrease in the density difference in the mixed convection region and (b) a reduction in the thermal conductivity due to the fluid transition from a liquid-like state to a vapor-like state.

3) The sharp increase in the Nusselt number in the heat transfer deterioration region is caused by the abrupt decrease in the thermal heat conductivity when the pseudo-critical point is crossed; this does not represent the real heat transfer capability but only the importance of heat convection relative to conduction.

4) The buoyancy force was found to have two opposing effects on the heat transfer. When $Bo^* \leq 4 \times 10^{-8}$, the forced convection is dominant, and the buoyancy force is negligible. The thermal flow acceleration and relaminarization of turbulence induced by the density reduction at the near-wall region cause the heat transfer deterioration. When $4 \times 10^{-8} < Bo^* \leq 8 \times 10^{-7}$, the natural convection starts to have a positive effect on the heat transfer and recovers part of the heat transfer ability. When $Bo^* > 8 \times 10^{-7}$, the natural convection is fully developed, and

the relaminarization of turbulence at the near-wall region is suppressed, which enhances the heat transfer.

5) Increasing the mass flux always leads to a higher heat transfer coefficient. When the bulk temperature is lower than the pseudo-critical temperature, increasing the heat flux enhances the heat transfer. However, when the bulk temperature is higher than the pseudo-critical temperature, increasing the heat flux cancels the heat transfer.

6) Based on the present experiments, two correlations of Nu for transcritical CO_2 convective heat transfer were developed, and both showed an acceptable deviation from the measured results. Geometric and structural factors should be considered in future studies in order to develop more widely applicable correlations.

Acknowledgements

Nomenclature

c_p	specific heat capacity
d	tube inner diameter (mm)
D	coil diameter (mm)
g	acceleration due to gravity (m/s^2)
G	mass flux (kg/m^2 s)
n	number of cross-section
Nu	Nusselt number
h	heat transfer coefficient (W/m^2 K)
H	enthalpy (kJ/kg)
I	electric current (A)
L	tube length (m)
p	coil pitch (mm)
P	fluid pressure (MPa)
Pr	Prandtl number
T	fluid temperature (K)
q	heat flux (kW/m^2)
Re	Reynolds number
U	voltage (V)
x	distance from tube inlet (m)

Greek symbols

ϕ	angle of circumference
μ	dynamic viscosity (Pa s)
ρ	density (kg/m^3)
η	thermal calibration
λ	thermal conductivity (W/m K)

Subscripts

b	bulk or buoyancy force
cal	calculated value
exp	experimental value
pc	pseudo-critical point
w	wall
in	inlet
inn	inner wall

References

[1] R.B. Duffey, I.L. Pioro, Experimental heat transfer of supercritical carbon dioxide flowing inside channels (survey), Nucl. Eng. Des. 235 (2005) 913–924.

[2] H.K. Oh, C.H. Son, New correlation to predict the heat transfer coefficient in-tube cooling of supercritical CO_2 in horizontal macro-tubes, Exp. Therm. Fluid Sci. 34 (2010) 1230–1241.

[3] D.E. Kim, M.H. Kim, Experimental investigation of heat transfer in vertical upward and downward supercritical CO_2 flow in a circular tube, Int. J. Heat Fluid Flow 32 (2011) 176–191.

[4] P.X. Jiang, Y. Zhang, R.F. Shi, Experimental and numerical investigation of convection heat transfer of CO_2 at supercritical pressures in a vertical mini-tube, Int. J. Heat Mass Transfer 51 (2008) 3052–3056.

[5] P.X. Jiang, R.F. Shi, C.R. Zhao, Y.J. Xu, Experimental and numerical study of convection heat transfer of CO_2 at supercritical pressures in vertical porous tubes, Int. J. Heat Mass Transfer 51 (2008) 6283–6293.

[6] Y.Y. Bae, H.Y. Kim, T.H. Yoo, Effect of a helical wire on mixed convection heat transfer to carbon dioxide in a vertical circular tube at supercritical pressures, Int. J. Heat Fluid Flow 32 (2011) 340–351.

[7] H.Z. Li, A. Kruizenga, M. Anderson, M. Corradini, Y.S. Luo, H.J. Wang, H.X. Li, Development of a new forced convection heat transfer correlation for CO_2 in both heating and cooling modes at supercritical pressures, Int. J. Therm. Sci. 50 (2011) 2430–2442.

[8] P. Naphon, S. Wongwises, A review of flow and heat transfer characteristics in curved tubes, Renew. Sust. Energ. Rev. 10 (2006) 463–490.

[9] N. Ghorbani, H. Taherian, M. Gorji, H. Mirgolbabaei, Experimental study of mixed convection heat transfer in vertical helically coiled tube heat exchangers, Exp. Therm. Fluid Sci. 34 (2010) 900–905.

[10] H.C. Kao, Torsion effect on fully developed flow in a helical pipe, J. Fluid Mech. 184 (1987) 335–356.

[11] S. Chingulpitak, S. Wongwises, Effects of coil diameter and pitch on the flow characteristics of alternative refrigerants flowing through adiabatic helical capillary tubes, Int. Commun. Heat Mass Transfer 37 (2010) 1305–1311.

[12] T.J. Huttl, R. Friedrich, Influence of curvature and torsion on turbulent flow in helically coiled pipes, Int. J. Heat Fluid Flow 21 (2000) 345–353.

[13] E.W. Lemmon, M.D. McLinden, M.L. Huber, Reference Fluid Thermodynamics and Transport Properties, NIST Standard Reference Database 23 (2010). Version 9.0.

[14] J. Taler, W. Zima, Solution of inverse heat conduction problem using control volume approach, Int. J. Heat Mass Transfer 42 (1999) 1123–1140.

[15] H.H. Ku, Notes on the use of propagation of error formulas, J. Res. Natl. Bur. Stand. 70C (1966) 262.

[16] A.N. Dravid, K.A. Smith, E.W. Merrill, et al., Effect of secondary fluid motion on laminar flow heat transfer in helically coiled tubes, AIChE J. 17 (1971) 1114–1122.

[17] R.C. Xin, M.A. Ebadian, The effects of Prandtl numbers on local and average convective heat transfer characteristics in helical pipes, J. Heat Transfer – ASME 119 (1997) 467–473.

[18] F. Merkel, Die Grundlagen der Warmeubertragung, Springer Publishing Company, Berlin, 1927.

[19] G.F.C. Rogers, Y.R. Mayhew, Heat transfer and pressure loss in helically coiled tubes with turbulent flow, Int. J. Heat Mass Transfer 7 (1964) 1207–1216.

[20] Y.M. Feng, W.C. Lin, C.C. Chieng, Numerically investigated effects of different Dean number and pitch size on flow and heat transfer characteristics in a helically coil-tube heat exchanger, Appl. Therm. Eng. 36 (2012) 378–385.

[21] C.Y. Yang, J.L. Xu, X.D. Wang, W. Zhang, Mixed convective flow and heat transfer of supercritical CO_2 in circular tubes at various inclination angles, Int. J. Heat Mass Transfer 64 (2013) 212–223.

[22] J.D. Jackson, M.A. Cotton, B.P. Axcel, Studies of mixed convection in vertical tubes, Int. J. Heat Fluid Flow 10 (1989) 2–15.

[23] D.M. McEligot, J.D. Jackson, "Deterioration" criteria for convective heat transfer in gas flow through non-circular ducts, Nucl. Eng. Des. 232 (2004) 327–333.

[24] W.S. Kim, C. Talbot, B.J. Chung, J.D. Jackson, Mixed convection heat transfer with variable properties to air flowing through a vertical passage of annular cross-section, Trans. Inst. Chem. Eng. A Chem. Eng. Res. Des. 80 (A) (2002) 239–245.

[25] C.H. Son, S.J. Park, An experimental study on heat transfer and pressure drop characteristics of carbon dioxide during gas cooling process in a horizontal tube, Int. J. Refrig. 29 (2006) 539–546.